Available online at www.sciencedirect.com
ScienceDirect
Ocean Modelling 15 (2006) 236–249
Ocean Modelling
www.elsevier.com/locate/ocemod

Pacific subtropical cell variability in coupled climate model simulations of the late 19th–20th century

Amy Solomon [a,*], Dongxiao Zhang [b]

[a] CIRES Climate Diagnostics Center, University of Colorado, and Physical Sciences Division/ NOAA Earth System Research Laboratory, Boulder, CO 80305, United States
[b] NOAA Pacific Marine Environmental Laboratory, Seattle, WA, United States

Received 28 June 2005; received in revised form 14 March 2006; accepted 22 March 2006
Available online 15 May 2006

Abstract

Observational studies of the Pacific basin since the 1950s have demonstrated that a decrease (increase) in tropical Pacific sea surface temperatures (SSTs) is significantly correlated with a spin-up (slow-down) of the Pacific Subtropical Cells (STCs). STCs are shallow wind-driven overturning circulations that provide a pathway by which extratropical atmospheric variability can impact the equatorial Pacific thermocline and, through upwelling in the eastern equatorial Pacific, tropical Pacific SSTs. Recent studies have shown that this observed relationship between SSTs and STCs is absent in coupled climate model simulations of the late 19th–20th centuries. In this paper we investigate what causes this relationship to breakdown and to what extent this limits the models' ability to simulate observed climate change in the equatorial Pacific since the late 19th century. To provide insight into these questions we first show that the NCAR Community Climate System Model's simulation of observed climate change since the 1970s has a robust signal in the equatorial Pacific that bears a close resemblance to observations. Strikingly, absent is a robust signal in the equatorial thermocline. Our results suggest that the coupled model may be reproducing the observed *local* ocean response to changes in forcing but inadequately reproducing the *remote* STC-forcing of the tropical Pacific due to the underestimate of extratropical winds that force these ocean circulations. These conclusions are found to be valid in five different coupled climate model simulations of the late 19th–20th centuries (CCSM3, GISS EH, GFDL CM2.1, CSIRO-Mk3, and HadCM3).

1. Introduction

Observed sea surface temperatures averaged over the tropical Pacific Ocean show a warming trend since the 1970s (e.g., Levitus et al., 2000). Changes in sea surface temperatures (SSTs) in the tropical Pacific have a profound impact on global climate (e.g., Trenberth et al., 1998). McPhaden and Zhang (2002) suggest that these changes are driven, in part, by transport variations in the Pacific Subtropical Cells (STCs), based on the observed correspondence between a decrease in transport convergence in the equatorial thermocline

* Corresponding author.
E-mail address: Amy.Solomon@noaa.gov (A. Solomon).

1463-5003/$ - see front matter
doi:10.1016/j.ocemod.2006.03.007

and an increase in tropical Pacific SSTs (their Fig. 2). The STCs are shallow meridional circulation cells in which water flows out of the tropics within the surface layer, subducts in the subtropics, flows equatorward within the thermocline, and upwells in the eastern equatorial ocean (Bryan, 1991, see his Fig. 2; McCreary and Lu, 1994; Liu et al., 1994; Blanke and Raynaud, 1997; Rothstein et al., 1996; Lu et al., 1998). The STCs provide a pathway by which extratropical atmospheric variability can force tropical variability through the ocean by temperature anomalies, T', that subduct in the extratropics and upwell at the equator (the VT' mechanism) (Gu and Philander, 1997) or by transport anomalies, V', that change the amount of water that upwells at the equator (the $V'T$ mechanism) (Kleeman et al., 1999).

Barnett et al. (2005) found that coupled climate models could only reproduce the observed warming of the Pacific SSTs when anthropogenic-forcings were included in the simulations. Zhang and McPhaden (this issue) analyzed the relationship between Pacific SSTs and STC transports in 18 model runs from 14 different coupled climate models forced with historical forcings. This study found that this observed relationship between SSTs and STCs is absent in coupled climate model simulations of the late 19th–20th centuries. In this paper we investigate what causes this relationship to breakdown and to what extent this limits the models' ability to simulate the climate of the late 19th–20th centuries. To provide insight into these questions we first analyze model data from the ocean component of the CCSM3 forced by observed heat fluxes and wind stress and five ensemble members of the CCSM3 forced with "historical" forcing for the period of 1958–1997. We then document to what extent an ensemble of five CCSM3 integrations reproduces the observed trend in the equatorial Pacific. We then assess to what extent the coupled model results differ from the uncoupled model results due to an inadequate representation of extratropical–tropical pycnocline water mass exchange.

It has been speculated that the observed climate trend after the 1970s and the increased warming of the world's oceans is due to an increase in anthropogenically-forced greenhouse gases (e.g., Washington and Meehl, 1996; Knutson and Manabe, 1998; Barnett et al., 2005). We isolate this signal in fully coupled climate models with the use of multiple integrations forced by the history of greenhouse gases from 1871 to 2000 (hereafter referred to as 20c3m forcings). We show that the conclusions and insights based on an analysis of the coupled and uncoupled NCAR models are valid in four additional fully coupled climate models (GISS EH, GFDL CM2.1, CSIRO–Mk3, and HadCM3).

2. Numerical models and observations used in this study

The terms "trend" and "variability" in this study refer to the difference between two 20-year averaged periods 1958–1977 (BEF77) and 1978–1997 (AFT78). These two periods have been chosen in order to compare the observed climate trend with model simulations of the late 19th–20th centuries. The BEF77 average is referred to as the reference climate mean state.

A detailed description of the NCAR models used in this study is provided in Solomon and Wainer (in press). This study uses five ensemble members of the CCSM3 (Collins et al., 2006) forced by 20c3m historical forcings. Four additional coupled climate system models are examined in this study, none of which are flux corrected:

(1) *GFDL CM2.1*: The NOAA Geophysical Fluid Dynamics Laboratory (GFDL) climate system model CM2.1 (Delworth et al., 2006) is run with a horizontal resolution of (2°NS × 2.5°EW) for the land and atmospheric components. The atmospheric model has 24 vertical levels. The ocean resolution is (1°NS × 1×EW), with meridional resolution equatorward of 30 becoming progressively finer, such that the meridional resolution is 1/3 at the Equator. There are 50 vertical levels in the ocean, with 22 evenly spaced levels within the top 220 m. The ocean component has poles over North America and Eurasia to avoid polar filtering. Three ensemble members are used in this study.
(2) *CSIRO Mk3*: The CSIRO Mk3 climate system model (Gordon et al., 2002) includes an AGCM run at (1.875°NS × 1.875°EW) resolution with 18 vertical levels. The ocean component is based upon the GFDL MOM2 code and is run at (0.9375°NS × 1.875°EW) with 31 vertical levels. Two ensemble members are used in this study.
(3) *GISS EH*: The NASA Goddard Institute for Space Studies climate system model EH (Hansen et al., 2002) is composed of the ModelE atmospheric code (internal version number E3), with horizontal

resolution of (5°NS × 4°EW) and 20 layers in the vertical, coupled to HYCOM (v. 0.9) with horizontal resolution of (2°NS × 2°EW) and 20 layers. Five ensemble members are used in this study.
(4) *HadCM3*: The United Kingdom Met Office Hadley Centre coupled climate system model HadCM3 (Gordon et al., 2000) has an atmospheric component run with a horizontal resolution of (2.5°NS × 3.75°EW) and 19 vertical levels. The ocean component is run with a horizontal resolution of (1.25°EW × 1.25°NS) and 20 vertical levels. Two ensemble members are used in this study.

POP is initialized in both the coupled and uncoupled models using January mean temperature and salinity fields (Levitus et al., 1998; Steele et al., 2001 in the Arctic Ocean) and a state of rest. The uncoupled POP3 simulation is forced by turbulent air–sea fluxes and wind stress calculated using atmospheric state data from the 1958–2000 global NCEP/NCAR reanalysis (Kalnay et al., 1996). This forcing is applied for three cycles; data from the last cycle of 40 years is presented in this paper. Radiative fluxes are calculated using the ISCCP (International Satellite Cloud Climatology Project) global radiative flux data products (Zhang et al., 2004). The climatological monthly mean GXGXS precipitation data set, constructed and documented by Large and Yeager (2004), is used to calculate freshwater fluxes. Under sea–ice, sea surface temperature and salinity are relaxed to observations. The details of this forcing and the resultant flux climatologies are documented in Large and Yeager (2004).

In a companion study, Solomon and Wainer (in press) found that POP forced with observed atmospheric conditions from the NCEP reanalysis over the period 1958–2000 has a realistic simulation of observed climate mean Pacific STCs. For example, the zonally averaged transport convergence at the equator in the subsurface branch of the climate mean STCs was well simulated. Since POP is the ocean component of the CCSM3 and since assimilated products of the ocean are dynamically unbalanced, we use the model output from this POP simulation as a proxy for observations.

3. STC variability in the NCAR models

3.1. The structure of the equatorial thermocline

3.1.1. Temperature

We begin our study by comparing the AFT78–BEF77 change in equatorial temperature structure from an ocean-alone simulation (POP) forced by observed heat fluxes and wind stress to five CCSM3 20c3m simulations (Fig. 1). Equatorial fields shown are averaged between 2°S and 2°N. The largest change in the POP simulation is found between 100 and 250 m deep from 120°E to 130°W, with maximum values of approximately 1.8 °C (Fig. 1a). Comparing Fig. 1a and b, it is seen that the negative anomalies in Fig. 1a are essentially an upward displacement of the equatorial thermocline from the base of the Warm Pool to the 15 °C isotherm. East of the dateline, warm anomalies surround the cold thermocline anomalies. These warm anomalies maximize in the mixed layer between 140°W and 120°W with anomalies greater than 1 °C.

There is seen to be a striking similarity between the uncoupled (Fig. 1a) and coupled (Fig. 1c) temperature differences east of the dateline, even though the ensemble mean CCSM3 anomalies are an order of magnitude smaller than the POP anomalies. In addition, equatorial SST differences do not exceed 0.4 °C in any of the individual ensemble members (results not shown). West of the dateline the anomalies from the CCSM3 ensemble mean deviate significantly from the POP simulation. Specifically, the ensemble mean shows a warming of the Warm Pool and essentially no change in the subsurface temperature structure. As a measure of the model's response to the change in forcing we calculate the signal to noise ratio. Following the IPCC Working Group 1 Third Assessment Report (Houghton, 2001), we calculate the signal to noise ratio as ensemble mean divided by the ensemble variance. We refer to a signal to noise ratio of 2:1, or two standard deviations (stds), as significant, a more conservative estimate than the one std used by the IPCC Third Assessment Report. It is seen that only the warming east of 140°W and west of 120°E in the CCSM3 have signal to noise ratios greater than two stds (Fig. 1d). These results indicate that, if there is a signal in the equatorial thermocline it is masked by the large variability among the integrations.

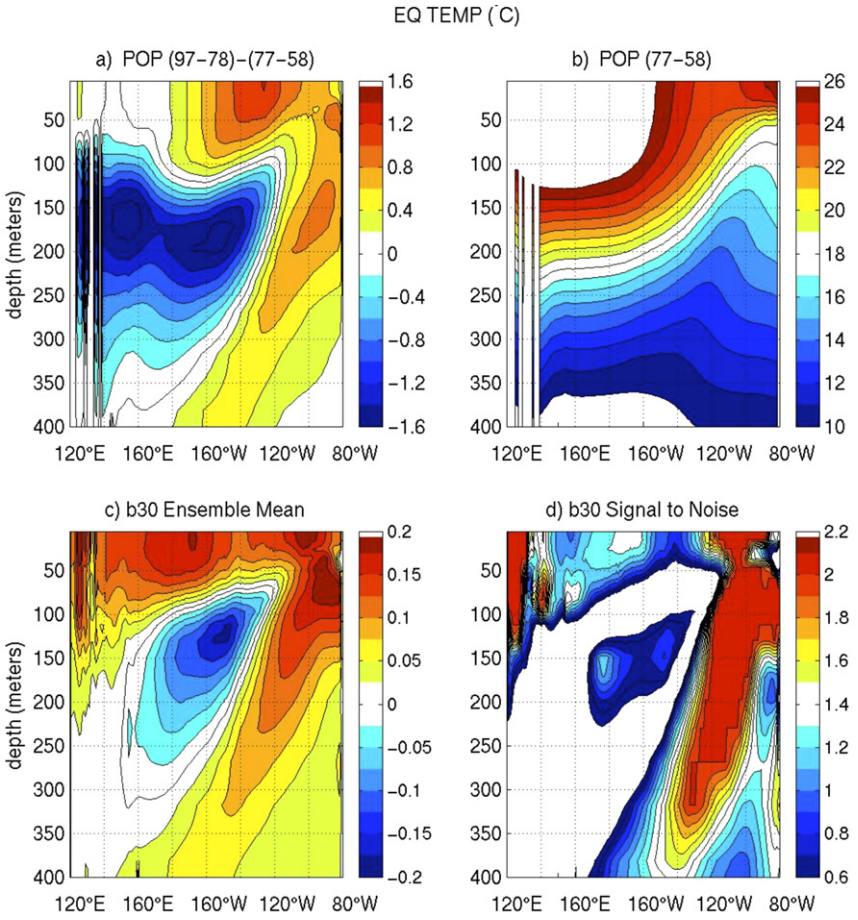

Fig. 1. Equatorial Pacific Ocean temperatures as a function of longitude and depth, in units of °C. (a) POP climate variability (1997–1978) minus (1977–1958), CI = 0.2. (b) POP climate mean (1977–1958), CI = 1. (c) CCSM3 ensemble mean climate variability, CI = .025. (d) CCSM3 ensemble signal to noise ratio, CI = 0.1.

3.1.2. Salinity

In Fig. 2 we compare the change in the equatorial salinity structure for the same model integrations, time periods and equatorial latitudes as described in Section 3.1.1. Below 100 m, regions of warming (seen in Fig. 1a) coincide with increased salinity and regions of cooling coincide with decreased salinity (Fig. 2a). Therefore, the salinity and temperature anomalies are partially density compensated. The change in equatorial density, however, has the same pattern as that seen for equatorial temperature change in Fig. 1a; increased density in regions of cooling ($>.25\ \mathrm{kg\ m^{-3}}$) and decreased density in regions of warming ($<-.1\ \mathrm{kg\ m^{-3}}$) (results not shown). The maximum density anomalies occur at and above the $25\ \mathrm{kg\ m^{-3}}$ climate mean isopycnal (figure not shown). Comparing Fig. 2a and b, it is seen the region of subsurface freshening occurs at and below the climate mean salinity maximum. Different from the small temperature anomalies in the Warm Pool seen in Fig. 1a, Fig. 2a shows a significant freshening of the Warm Pool after the 1970s.

The freshening of the Warm Pool observed in the POP simulation is also seen in the ensemble mean (Fig. 2c); again the CCSM3 ensemble mean anomalies are an order of magnitude smaller than those from the POP simulation. However the freshening of the equatorial thermocline and the increased salinity in the eastern Pacific, seen in the POP simulation, are absent in the CCSM3 ensemble mean. The signal to noise ratio plotted in Fig. 2d shows that there are no salinity anomalies with signal to noise ratios greater than two stds. Therefore, the freshening of the Warm Pool is not a robust feature of the CCSM3 integrations and if there is a signal in this region it is significantly smaller than the variability between the integrations.

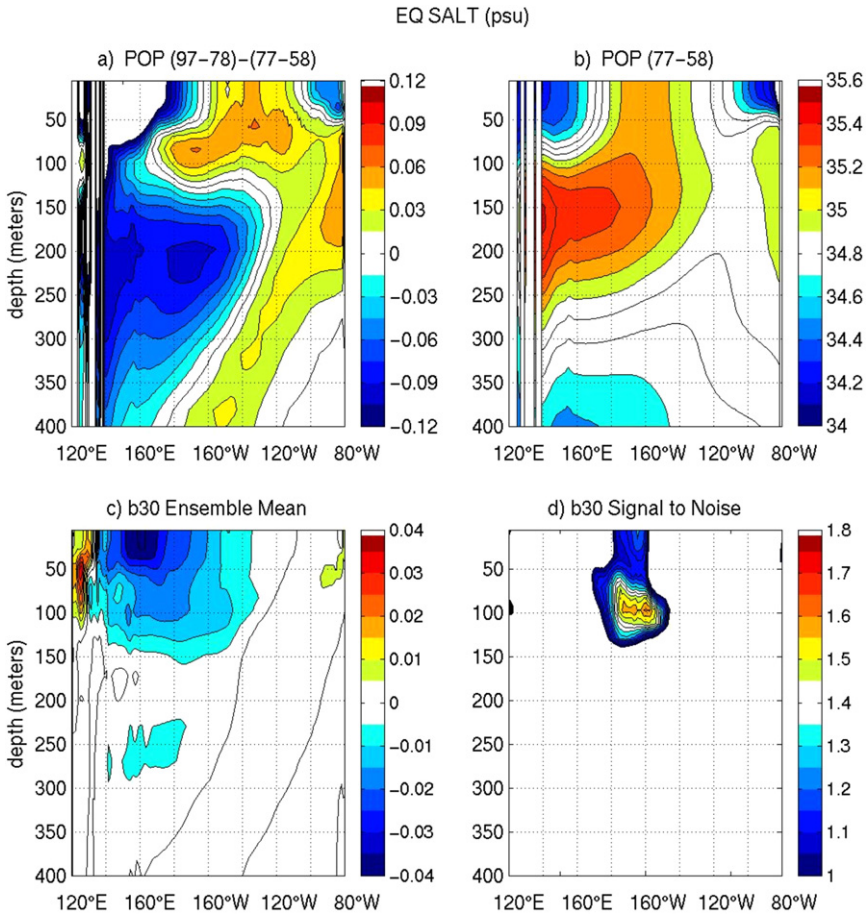

Fig. 2. Equatorial Pacific Ocean salinity as a function of longitude and depth, in units of psu. (a) POP climate variability (1997–1978) minus (1977–1958), CI = .015. (b) POP climate mean (1977–1958), CI = .1. (c) CCSM3 ensemble mean climate variability, CI = .005. (d) CCSM3 ensemble signal to noise ratio, CI = .05.

3.1.3. Summary

Interestingly, the CCSM3 ensemble mean difference between AFT78 and BEF77 reproduces the *structure* of the observed warming of the eastern equatorial Pacific, the cooling of the thermocline in the central Pacific, and the freshening of the Warm Pool. However, the subsurface cooling in the western Pacific and the salinity anomalies in the equatorial pycnocline are absent in the ensemble mean. In this rest of the paper we investigate to what extent this absence is due to an inadequate representation of extratropical–tropical pycnocline water mass exchange in the coupled models. We will determine whether the weak signal in the CCSM3's simulation of equatorial pycnocline variability is related to the coupled model's simulation of the forcing of pycnocline transports.

3.2. Surface Pacific decadal variability: the forcing of the Pacific STCs

3.2.1. SST

The POP simulation of observed SST variability (AFT78-BEF77) tends to overestimate the warm SST anomalies in the equatorial eastern Pacific (Fig. 3a). However, the wedge of warm SSTs extending from 160°E, 0–40° near the eastern boundary in both the North and South Pacific, with cold anomalies poleward, is well simulated. Relative to the climate mean SSTs (Fig. 3b), the warm anomalies in the eastern equatorial

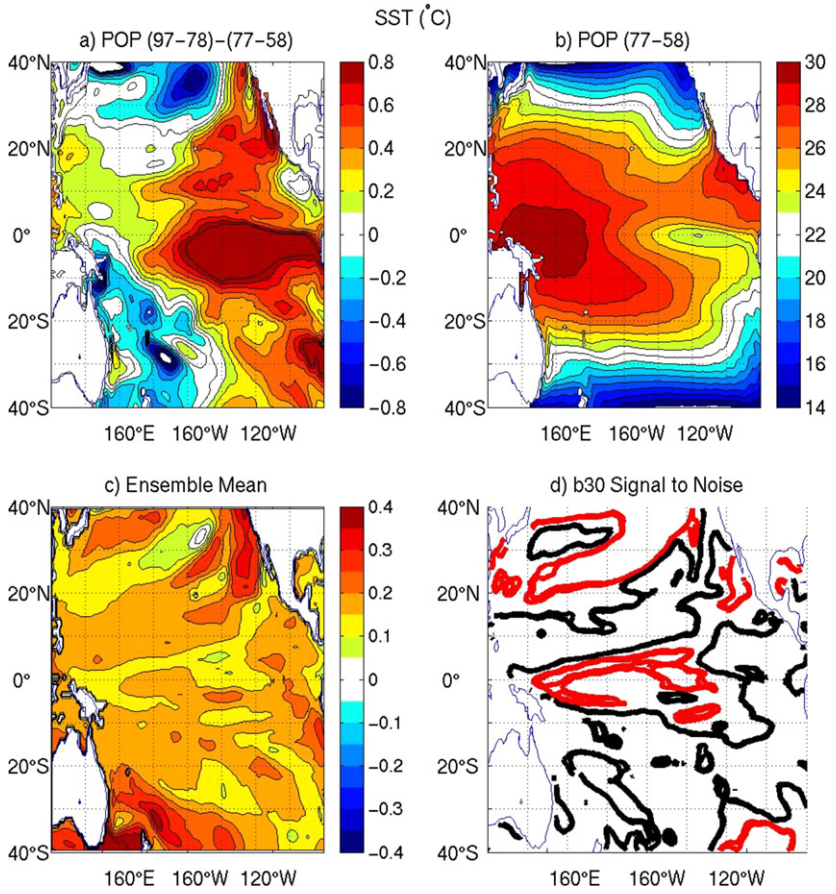

Fig. 3. Pacific Ocean sea surface temperature as a function of longitude and latitude, in units of °C. (a) POP climate variability (1997–1978) minus (1977–1958), CI = .1. (b) POP climate mean (1977–1958), CI = 1. (c) CCSM3 ensemble mean climate variability, CI = .05. (d) CCSM3 ensemble signal to noise ratio, one std = red, two stds = black.

Pacific warm the cold tongue at and south of the equator. There are two secondary regions of warm SST anomalies near the eastern boundary of the tip of Baja California and off the coast of Chile near 30°S.

The observed pattern of SST anomalies is not seen in the CCSM3 ensemble mean SSTs (Fig. 3c). Even though the ensemble mean shows a broad-scale warming in the tropical Pacific, similar to observations, the subtropical cold anomalies are absent and the warm anomalies are a maximum in the subtropics not in the cold tongue region. The ensemble mean SST anomalies are of the same order as SST anomalies in the POP simulation except for SST anomalies in the cold tongue region. The signal to noise ratio (Fig. 3d) exceeds two stds (the black contours) in most of the basin except for the tropical Pacific west of 120°W and in the North Pacific where ensemble mean anomalies are less than 0.15 °C.

3.2.2. Surface winds

In Fig. 4 we plot the extra-equatorial Ekman pumping (absolute values greater than 8×10^{-6} m/s in the mean and 2×10^{-6} m/s in variability are masked out). Ekman pumping is calculated as, $w_e = -\mathrm{curl}(\boldsymbol{\tau}/\rho_0 f)$, where $\boldsymbol{\tau}$ is the vector wind stress, f is the Coriolis parameter, and ρ_0 is a constant reference density (10^3 kg m^{-3}).

Maximum climate mean Ekman pumping in the ocean-alone simulation is seen throughout the tropics away from the western boundary (Fig. 4b). However, it is the Ekman pumping in the subtropics that we focus on since this is where isopycnals that intersect the upper equatorial pycnocline outcrop, approximately between 18° and 23° latitude (Qiu and Huang, 1995; Huang and Qiu, 1998; Karstensen and Quadfasel,

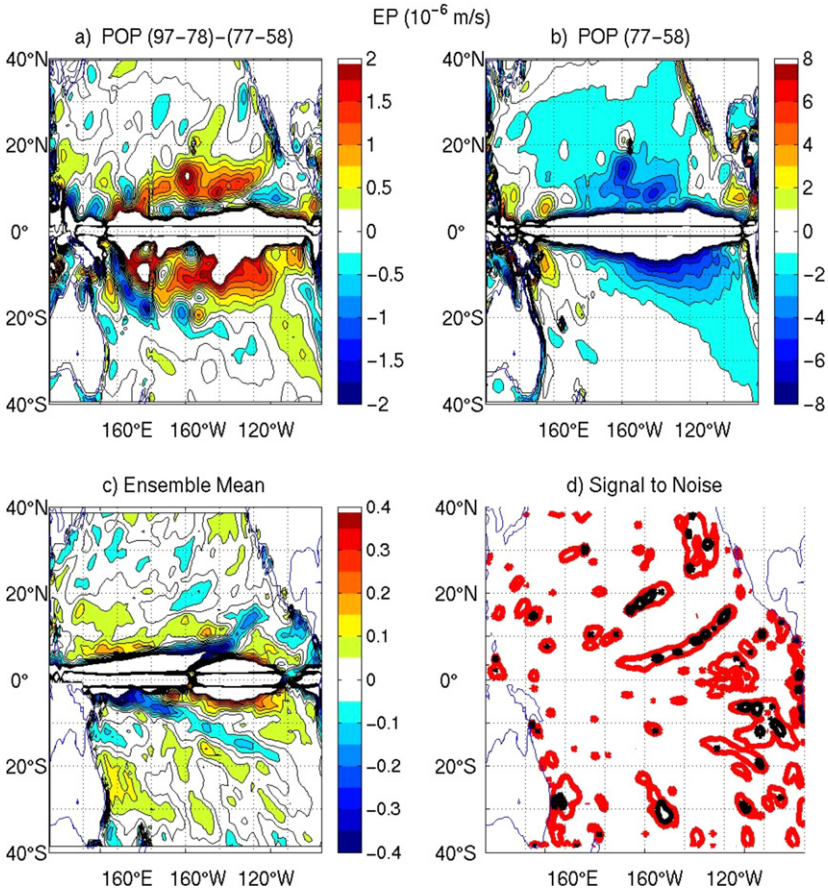

Fig. 4. Pacific Ocean Ekman pumping as a function of longitude and latitude, in units of m $s^{-1} \times 10^{-6}$. (a) POP climate variability (1997–1978) minus (1977–1958), CI = .25. (b) POP climate mean (1977–1958), CI = 1. (c) CCSM3 ensemble mean climate variability, CI = .05. (d) CCSM3 ensemble signal to noise ratio, one std = red, two stds = black.

2002). In the subtropical North Pacific, climate mean Ekman pumping is observed across the basin. By contrast, climate mean Ekman pumping of magnitude larger than 1×10^{-6} m/s only exists in a limited region near the eastern boundary in the subtropical South Pacific.

The largest change in Ekman pumping observed since the 1970s occurs within the tropics except for the region north and east of Hawaii and in the subtropical South Pacific in the region of maximum climate mean Ekman pumping (Fig. 4a). Ekman pumping is reduced in the eastern Pacific (where isopycnals that intersect the equatorial thermocline outcrop, near 17°S, 120°W and 20°N, 160°W), suggesting that the observed slowdown of the STCs since the 1970s is related to a reduction in the wind forcing at the poleward edge of the cells.

A reduction in Ekman pumping within the tropics is seen in the CCSM3 ensemble mean (Fig. 4c) but it tends to be more narrowly confined near the equator and is an order of magnitude smaller than the change in POP. In addition, the signal to noise ratio in the basin only exceeds two stds in very limited areas such as near Hawaii and in the eastern South Pacific near 10°S (Fig. 4d).

Given the lack of a clear signal in the wind field, what then is driving the systematic change in CCSM3 ocean temperature see in Figs. 1 and 3? Given the high degree of noise in the surface winds, it is most likely necessary to use more than five simulations to separate the signal from the noise. However, none of the CCSM3 simulations have Ekman pumping anomalies at the poleward edge of the tropics of the order of observations (results not shown), an indication that the coupled model is underestimating extra-equatorial decadal wind variability. In the next section we focus our analysis on subsurface fields that are not in direct

contact with the atmosphere except in the outcropping region. Given that these fields are shielded from the highly variable atmospheric fields we expect to find a higher signal to noise ratio.

3.3. Subsurface Pacific decadal variability: Pacific STC variability

3.3.1. Salinity on the 25 kg m^{-3} surface

Water with densities between 22–26 kg m^{-3} in the North Pacific and 22.5–26.2 kg m^{-3} in the South Pacific flows along isopycnal pathways to the tropical thermocline (Johnson and McPhaden, 1999; MZ02). The 25 kg m^{-3} isopycnal surface intersects the core of the EUC at the equator in the ocean-alone and coupled models used in this study (results not shown). Therefore, we plot salinity on the 25 kg m^{-3} surface to identify extratropical sources of equatorial thermocline water. On the 25 kg m^{-3} isopycnal surface large-scale potential vorticity contours coincide with salinity contours (results not shown), indicating that eastern subtropical mode waters contribute to the subsurface equatorward branches of the STCs. Salinity maxima are seen in the central North and South Pacific (22°N, 160°W and 20°S, 120°W) in the region of the winter outcropping lines, indicated by the poleward edges of the contours. (Fig. 5b). Since the 1970s, the salinity of water that subducts in the North and South Pacific has deceased. This variability is seen to extend to the western boundary in both the North and South Pacific and along (and to the north of) the equator (Fig. 5a). Consistent with the CCSM3's underestimate of STC wind forcing (discussed in Section 3.2.2), the change in the strength of the

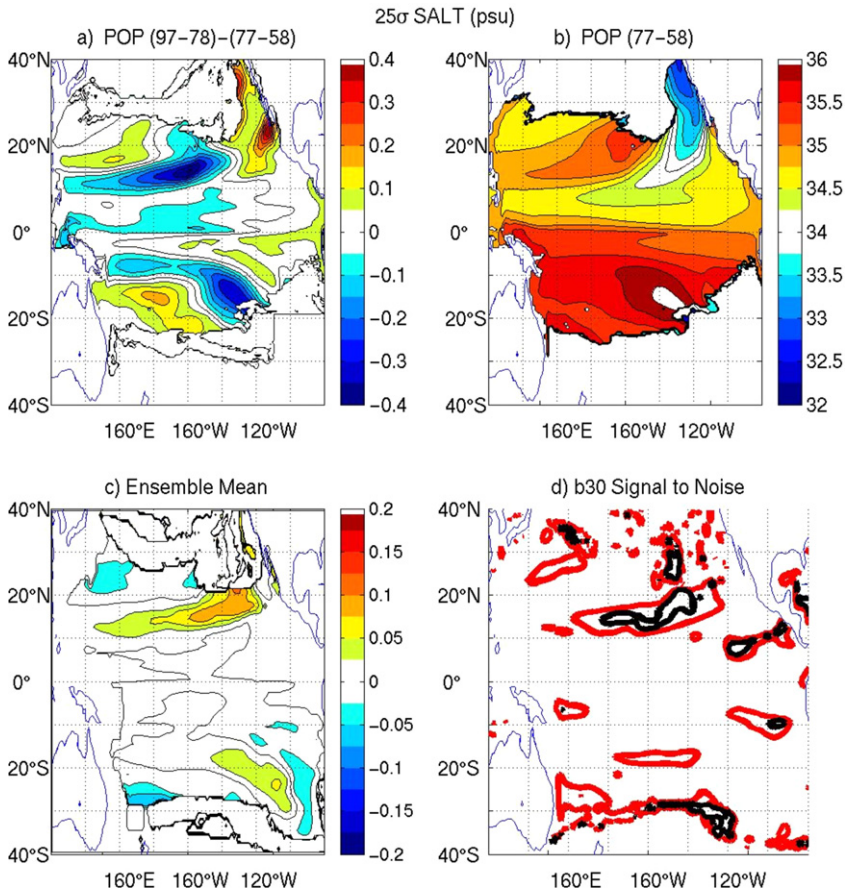

Fig. 5. Pacific Ocean salinity on the isopycnal surface that intersects the equator at the core of the thermocline (25 kg m^{-3}) as a function of longitude and latitude, in units of psu. (a) POP climate variability, (1997–1978) minus (1977–1958), CI = .1. (b) POP climate mean (1977–1958), CI = .25. (c) CCSM3 ensemble mean climate variability, CI = .025. (d) CCSM3 ensemble signal to noise ratio, one std = red, two stds = black.

STCs is too weak for salinity variability initiated at the wintertime outcropping lines to reach the equator (Fig. 5c).

3.3.2. Meridional pycnocline transports

The POP climate mean interior meridional transport integrated between 24 and 26 kg m^{-3} and the change in these transports since the 1970s are plotted in Fig. 6b and a, respectively. The climate mean transport initiated at the winter outcropping lines (indicated by the poleward boundaries of the contours in Fig. 5b) flows to the equator in both the North and South Pacific (Fig. 6b). However, near 5°N and 5°S the transports are significantly reduced from transports poleward. This indicates that either water transported into the area is mixed upwards or water is diverted away from the equator.

The change in POP interior pycnocline transports since the 1970s shows a decrease of >25% from the outcropping lines to the equator in both the North and South Pacific, in agreement with the observational study of MZ02 (Fig. 6a). This change in transports is of the same order in both the North and South Pacific, with a maximum change south of Hawaii in the North Pacific and north of the Marquises in the South Pacific. There is a consistent change in transports from the wintertime outcropping lines to the equator, i.e., a decrease in equatorward transports by the subsurface branches of the STCs.

The CCSM3 ensemble mean change in interior pycnocline transports and the signal to noise ratio among the five simulations is plotted in Fig. 6c and d. In the North Pacific, different from the POP simulation, interior transports increase south of Hawaii but decrease just north of the equator. Looking at Fig. 6d, both the region south of Hawaii and just north of the equator have signal to noise rations greater than two stds. Only the

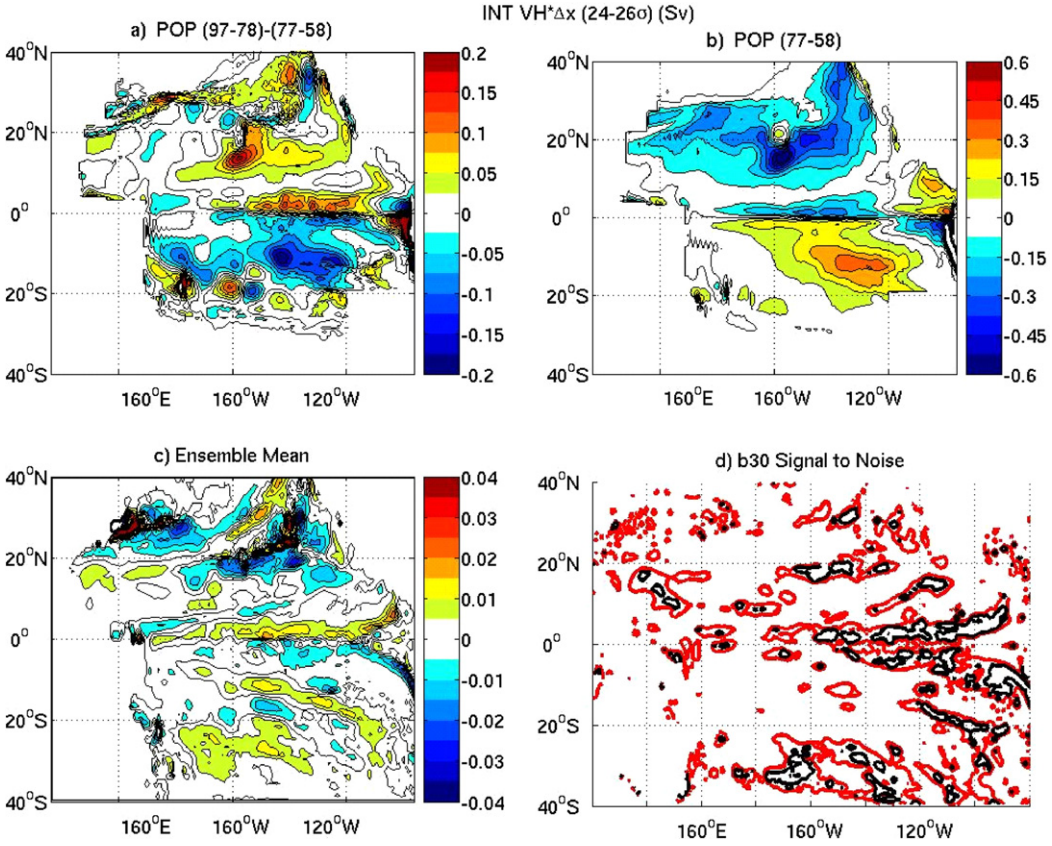

Fig. 6. Pacific Ocean interior pycnocline transport ($VH * \Delta x$) as a function of longitude and latitude, in units of Sv. (a) POP climate variability, (1997–1978) minus (1977–1958), CI = .025. (b) POP climate mean (1977–1958), CI = .075. (c) CCSM3 ensemble mean climate variability, CI = .005. (d) CCSM3 ensemble signal to noise ratio, one std = red, two stds = black.

subtropical increase and the near-equatorial decreases in the eastern South Pacific have signal to noise ratios greater than two stds. There is no clear relationship between the change in transports near the outcropping lines and the near-equatorial transports as was found in the POP simulation (Fig. 6a). However, it is interesting to note that the decrease in near-equatorial pycnocline convergence is consistent with the increase in eastern equatorial SSTs, indicating that changes in easterly trade winds are impacting equatorial SSTs by modifying transport into the equatorial zone (McCreary and Lu, 1994; Nonaka et al., 2002).

4. Comparison with other coupled models

In Section 3 we demonstrated that the CCSM3's simulation of observed climate variability since the 1970s produced a warming of the tropical Pacific consistent with observation. However, it is important to note that the model produced a uniform warming of the Pacific Ocean unlike observations. To assess if this is a robust result among a range of climate models (and to compare with the observational study of MZ02) we plot AFT78–BEF77 SSTs averaged in the eastern tropical Pacific (9°N–9°S, 90°W–180°W) in Fig. 7. The 0.6 °C warming of the tropical Pacific simulated by the POP simulation is consistent with the estimate of 0.8 °C by MZ02. A warming of the tropical Pacific is produced by all of the coupled models, however all the models underestimate the magnitude of the observed warming. In addition, Fig. 7 shows that there is a wide range of climate mean tropical SSTs among the coupled models due to different simulations of the eastern Pacific "Cold Tongue".

MZ02 found that the wind forcing of the surface branch of the STCs weakened after the 1970s. This weakening was found to be comparable to the estimated decrease in interior pycnocline transport convergence. To determine if this weakening of the wind forcing of the STCs and the interior pycnocline transport convergence are robust among the coupled models, and to compare with MZ02, we plot the divergence of the AFT78–BEF77 Ekman transport integrated across 9°N and 9°S, $ET = \int [M_e(9°N) - M_e(9°S)]dx$ in Fig. 8 and the interior pycnocline transport convergence between 9°N and 9°S (VH2426) in Fig. 9. M_e is calculated following MZ02 as, $M_e = -\tau_x/\rho_0 f$, where τ_x is the zonal component of the wind stress, f is the Coriolis parameter, and ρ_0 is a constant reference density (10^3 kg m^{-3}). ET from the POP simulation is seen to decrease from 67 Sv to 53 Sv after the 1970s, consistent with the observed estimates of MZ02. All of the coupled models underestimate this change in the wind forcing of the STCs – there is essentially no change in the wind forcing after the 1970s. This is the case for the ensemble means as well as the individual ensemble members (results not shown). As was found by MZ02, there is a comparable decrease in the interior pycnocline transport convergence in the POP simulation (Fig. 9). This change (in all of the coupled models except GISS EH) is an order of

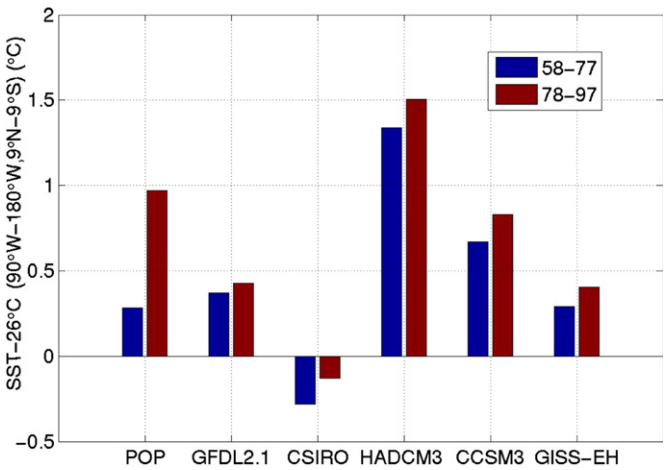

Fig. 7. Sea surface temperature averaged over the eastern tropical Pacific (90°W–180°W, 9°N–9°S) in units of °C (−26 °C to highlight the variability), for POP and five coupled climate models forced with observed forcing. Climate mean averages for (1958–1977) = blue and (1978–1997) = red.

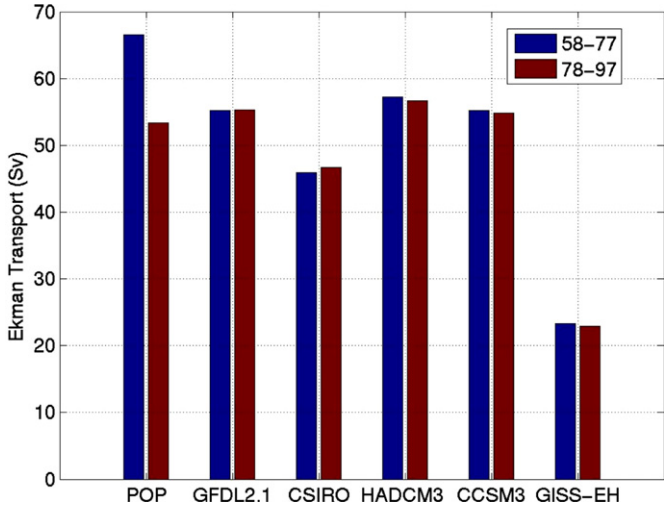

Fig. 8. Ekman transport divergence (9°N − 9°S) integrated from the eastern boundary to near the western boundary, in units of Sv, for POP and five coupled climate models forced with observed forcing. Climate mean averages for (1958–1977) = blue and (1978–1997) = red.

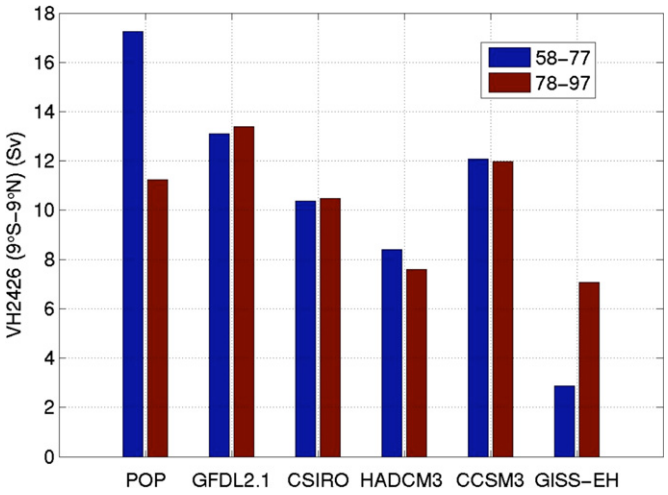

Fig. 9. Interior pycnocline convergence, 9°S − 9°N, summed between 24 and 26 kg m^{-3}, in units of Sv, for POP and five coupled climate models forced with observed forcing. Climate mean averages for (1958–1977) = blue and (1978–1997) = red.

magnitude smaller than the POP simulation. In addition, there is no consistency in the sign of this change. It is also important to note that the climate mean VH2426 in the coupled models is at least 4 Sv smaller than the POP simulation, suggesting that the climate mean forcing of the STCs is also underestimated.

Section 3 showed that changes in salinity along the 25 kg m^{-3} density surface since the 1970s extend from North and South Pacific outcropping regions to the equatorial thermocline in the POP simulation but only extend to within 10° of the equator in the CCSM3 integrations (Fig. 5). To see if this result is valid among the four additional coupled models we plot the change in salinity on the 25 kg m^{-3} density surface averaged over (120°E–140°W, 5°N–5°S) in Fig. 10. This figure clearly shows that all of the coupled models underestimate the observed change in salinity within 5° of the equatorial thermocline. This is again an indication that the forcing of the tropical Pacific by extratropical atmospheric variability through the subsurface branch of the STCs is underestimated in all of the coupled climate models included in this study.

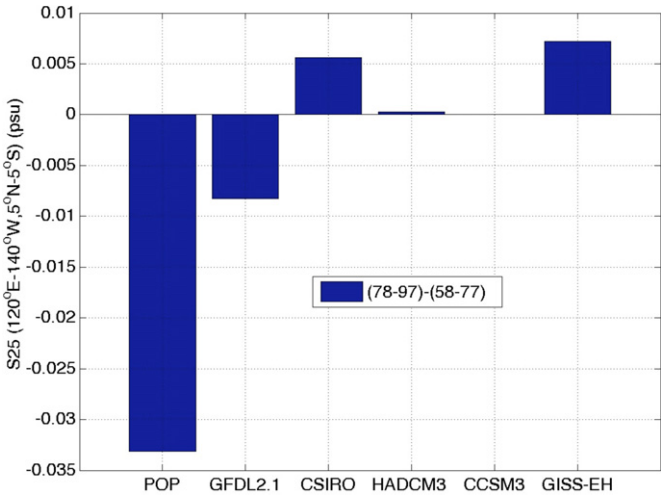

Fig. 10. Western–central equatorial (120°E–140°W, 5°N–5°S) salinity change since the 1970s on the 25 kg m^{-3} isopycnal, in units of psu, for POP and five coupled climate models forced with observed forcing. Climate mean averages for (1958–1977) = blue and (1978–1997) = red.

5. Summary and discussion

Recent studies, most notably Meehl et al. (2004), have shown that the rapid warming of global surface temperature after the mid-1970s is more a result of global warming than natural variability. In addition, Zhang and McPhaden (this issue) analyzed the 20c3m simulations to find that the tropical Pacific SST trend is significantly correlated with the simulated global mean surface temperature, suggesting that the modeled SST trend is forced by global warming, but without involving changes in STC transports. In this paper we investigated what causes this relationship to breakdown and to what extent this limits the models' ability to simulate the climate of the late 19th–20th centuries. We used the two 20-year periods across 1977 to estimate Pacific basin changes under global warming conditions. We found that there is essential no change in the analyzed 20c3m simulations as large as in the observed tropical Pacific SST. This result suggests that the 20c3m simulations underestimate the trend in SST under global warming conditions. It is important to note here that our results can only be suggestive; since it is unclear to what extent the observed trend in the tropical Pacific is due to internal multi-decadal variability.

In the first half of this paper we demonstrated that the CCSM3's simulation of observed climate change since the 1970s has a robust signal in the equatorial Pacific with a pattern that bears close resemblance to observations. This signal is a warming of the equatorial SSTs, a warming of the lower thermocline in the eastern equatorial Pacific and a cooling of the upper thermocline in the central Pacific. What is conspicuously absent in the CCSM3 simulation is the observed cooling of the thermocline in the western to central equatorial Pacific. Since this variability occurs in the equatorial thermocline, where the water mass properties indicate a subtropical source, we then explored to what extent this discrepancy is due to inadequate representations of extratropical–tropical water mass exchange in the Pacific basin.

Looking first at the surface fields it was then shown that, even though the CCSM3 and POP equatorial variability have similarities, the basin-wide surface fields are completely different. Notably, POP's SSTs warm in the equatorial and eastern subtropics and cool in the western subtropics, while the CCSM3 has a uniform warming in the basin. In addition, we showed that the CCSM3's Ekman pumping variability away from the equator is an order of magnitude smaller than the POP model output. The extra-equatorial variability from the POP simulation is not seen in any individual CCSM3 ensemble member, suggesting that the coupled model is underestimating the extra-equatorial wind variability. We conclude from these results that the forcing of Pacific STC variability through extratropical atmospheric variability is underestimated in the CCSM3.

An analysis of salinity on the 25 kg m^{-3} surface from the POP simulation indicated that less saline water subducts in the extratropics and flows to the equator since the 1970s. This reduction in salinity is seen in water masses that flow from the extratropics to the western boundary, in both hemispheres, and then along the equator. In the CCSM3, salinity variability only extended to within 10° of the equator, consistent with the lack of a signal in the ensemble mean equatorial thermocline. The POP simulation produced changes in interior pycnocline transports consistent with observation, a greater than 25% decrease in equatorward pycnocline transport in both hemispheres from the outcropping region to the equator. Interestingly, even though the CCSM3 integrations did not reproduce this observed tropics-wide reduction in equatorward transport, they produce a reduction in eastern equatorial pycnocline convergence and a coincident increase in equatorial SSTs. These results suggest that the coupled model may be reproducing the observed *local* ocean mixed layer response to changes in forcing but inadequately reproducing the *remote* forcing of the tropical Pacific through STC variability because the extratropical winds that force these ocean circulations are underestimated.

In Section 4 we demonstrated that the conclusions based on a comparison between the POP simulation and the CCSM3 ensemble are robust among five different coupled climate model simulations. In short, we found that all models simulate a warming of the tropical Pacific after the 1970s. This warming was an order of magnitude smaller than observations. Using salinity as a tracer, we demonstrated that, unlike observations, this warming occurs without any indication that the models' extratropical surface winds are significantly impacting the equatorial Pacific through the subsurface branch of the STCs.

Acknowledgements

We thank the Oceanography and Climate Modeling Divisions at the National Center for Atmospheric Research, Shan Sun at the NASA Goddard Institute for Space Studies, and the NOAA Geophysical Fluid Dynamics Laboratory Climate Modeling group, for providing coupled model output analyzed in this study. We acknowledge the international modeling groups for providing their data for analysis, the Program for Climate Model Diagnosis and Intercomparison (PCMDI) for collecting and archiving the model data, the JSC/CLIVAR Working Group on Coupled Modelling (WGCM) and their Coupled Model Intercomparison Project (CMIP) and Climate Simulation Panel for organizing the model data analysis activity, and the IPCC WG1 TSU for technical support. The IPCC Data Archive at Lawrence Livermore National Laboratory is supported by the Office of Science, US Department of Energy. We thank two thoughtful reviewers and Mike Alexander for comments on the manuscript. A.S. and D.Z. acknowledge the support of the NOAA Climate Program Office and the Office of Global Programs as a Climate Model Evaluation Project (CMEP) under the US CLIVAR Program.

References

Barnett, T.P., Pierce, D.W., Achuta Rao, K.M., Gleckler, P.J., Santer, B.D., Gregory, J.M., Washington, W.M., 2005. Penetration of human-induced warming into the world's oceans. Science 309, 284–287.

Blanke, B., Raynaud, S., 1997. Kinematics of the Pacific Equatorial undercurrent: an Eulerian and Lagrangian approach from GCM results. J. Phys. Oceanogr. 17, 1038–1053.

Bryan, K., 1991. Poleward heat transport in the ocean. Tellus 43, 104–115.

Collins, W.D., Bitz, C.M., Blackmon, M.L., Bonan, G.B., Bretherton, C.S., Carton, J.A., Chang, P., Doney, S.C., Hack, J.J., Henderson, T.B., Kiehl, J.T., Large, W.G., McKenna, D.S., Santer, B.D., Smith, R.D., 2006. The community climate system model: CCSM3. J. Climate 19, 2122–2143.

Delworth, T.L., Broccoli, A.J., Rosati, A., Stouffer, R.J., Balaji, V., Beelsey, J.A., Cooke, W.F., Dixon, K.W., Dunne, J., Dunne, K.A., Durachta, J.W., Findell, K.L., Ginoux, P., et al., 2006. GFDL's CM2 global coupled climate models. Part I: Formulation and simulation characteristics. J. Climate 19, 643–674.

Gordon, C., Cooper, C., Senior, C.A., Banks, H., Gregory, J.M., Johns, T.C., Mitchell, J.F.B., Wood, R.A., 2000. The simulation of SST, sea ice extents and ocean heat transports in a version of the Hadley Centre Coupled Model without flux adjustments. Climate Dyn. 16, 147–168.

Gordon, H.B., Rotstayn, L.D., McGregor, J.L., Dix, M.R., Kowalczyk, E.A., O'Farrell, S.P., Waterman, L.J., Hirst, A.C., Wilson, S.G., Collier, M.A., Watterson, I.G., Elliott, T.I., 2002. The CSIRO Mk3 Climate System Model. CSIRO Atmospheric Research Technical Paper No. 60.

Gu, D., Philander, S.G.H., 1997. Interdecadal climate fluctuations that depend on exchanges between the tropics and the extratropics. Science 275, 805–807.

Hansen, J.E., Sato, M., Nazarenko, L., Ruedy, R., Lacis, A., Tegen, I., Hall, T., Shindell, D., Stone, P., Novakov, T., Thomason, L., Wang, R., Wang, Y., Jacob, D.J., Hollandsworth-Frith, S., Bishop, L., Logan, J., Thompson, A., Stolarski, R., Lean, J., Willson, R., Levitus, S., Antonov, J., Rayner, N., Parker, D., Christy, J., 2002. Climate forcings in Goddard Institute for Space Studies SI2000 simulations. J. Geophys. Res. 107, 4347. doi:10.1029/2001JD001143.

Houghton, J.T., Intergovernmental Panel on Climate Change. Working Group I, 2001. Climate Change 2001: The Scientific Basis: contribution of Working Group I to the third assessment report of the Intergovernmental Panel on Climate Change. Cambridge University Press, Cambridge, UK.

Huang, R.X., Qiu, B., 1998. The structure of the wind-driven circulation in the subtropical South Pacific. J. Phys. Oceanogr. 28, 1173–1186.

Johnson, G.C., McPhaden, M.J., 1999. Interior pycnocline flow from the subtropical to the equatorial Pacific Ocean. J. Phys. Oceanogr. 29, 3073–3089.

Kalnay, E., Kanamitsu, M., Kistler, R., Collins, W., Deaven, D., Gandin, L., Iredell, M., Saha, S., White, G., Woollen, J., Zhu, Y., Chelliah, M., Ebisuzaki, W., Higgins, W., Janowiak, J., Mo, K., Ropelewski, C., Leetmaa, A., Reynolds, R., Jenne, R., 1996. The NCEP/NCAR 40-year reanalysis project. Bull. Am. Met. Soc. 77, 437–471.

Karstensen, J., Quadfasel, D., 2002. Formation of southern hemisphere thermocline waters: water mass conversion and subduction. J. Phys. Oceanogr. 32, 3020–3038.

Kleeman, R., McCreary, J.P., Klinger, B.A., 1999. A mechanism for the decadal variation of ENSO. Geophys. Res. Lett. 26, 743–747.

Knutson, T.R., Manabe, S., 1998. Model assessment of decadal variability and trends in the Tropical Pacific Ocean. J. Climate 11, 2273–2296.

Large, W.G., Yeager, S.G., 2004. Diurnal to decadal global forcing for ocean and sea–ice models: the data sets and flux climatologies. NCAR Technical Note NCAR/TN-460+STR, 111 pp.

Levitus, S., Boyer, T., Conkright, M., Johnson, D., O'Brien, T., Antonov, J., Stephens, C., Gelfeld, R., 1998. World Ocean Database 1998 Volume 1: Introduction. NOAA Atlas NESDIS 18. US Government Printing Office, Washington, DC, 346 pp.

Levitus, S., Antonov, J.I., Boyer, T.P., Stephens, C., 2000. Warming of the World Ocean. Science 287, 2225–2229.

Liu, Z., Philander, S.G.H., Pacanowski, R.C., 1994. A GCM study of tropical–extratropical upper ocean water exchange. J. Phys. Oceanogr. 24, 2606–2623.

Lu, P., McCreary, J.P., Klinger, B., 1998. Meridional circulation cells and the source waters of the Pacific equatorial undercurrent. J. Phys. Oceanogr. 28, 62–84.

McCreary, J., Lu, P., 1994. On the interaction between the subtropical and the equatorial oceans: the subtropical cell. J. Phys. Oceanogr. 24, 466–497.

McPhaden, M.J., Zhang, D., 2002. Slowdown of the meridional overturning circulation in the upper Pacific Ocean. Nature 415, 603–608.

Meehl, G.A., Washington, W.M., Ammann, C.M., Arblaster, J.M., Wigley, T.M.L., Tebaldi, C., 2004. Combinations of natural and anthropogenic forcings in twentieth century climate. J. Climate 17, 3721–3727.

Nonaka, M., Xie, S.-P., McCreary, J., 2002. Decadal variations in the subtropical cells and equatorial Pacific SST. Geophys. Res. Lett. 29. doi:10.1029/2001GL013717.

Qiu, B., Huang, R.X., 1995. Ventilation of the North Atlantic and North Pacific: subduction vs obduction. J. Phys. Oceanogr. 25, 2374–2390.

Rothstein, L.M., Zhang, R.-H., Busalacchi, A.J., Chen, D., 1996. A numerical simulation of the mean water pathways in the subtropical and tropical Pacific Ocean. J. Phys. Oceanogr. 28, 322–344.

Solomon, A., Wainer, I., in press. Pacific tropical–extratropical thermocline water mass exchanges in the NCAR coupled climate system model, version 3. Ocean Model. (special issue), doi:10.1016/j.ocemod.2006.04.003.

Steele, M., Morley, R., Ermold, W., 2001. PHC: A global ocean hydrography with a high quality Arctic Ocean. J. Climate 14, 2079–2087.

Trenberth, K.E., Branstator, G.W., Karoly, D., Kumar, A., Lau, N.-C., Ropelewski, C., 1998. Progress during TOGA in understanding and modeling global teleconnections associated with tropical sea surface temperatures. J. Geophys. Res. 103, 14291–14324.

Washington, W.M., Meehl, G.A., 1996. High latitude climate change in a global coupled ocean–atmosphere–sea ice model with increased atmospheric CO_2. J. Geophys. Res. 101, 12795–12801.

Zhang, D., McPhaden, M.J., this issue. Decadal variability of the shallow Pacific meridional overturning circulation and its relation to tropical sea surface temperatures in observations and climate change models. Ocean Model (special issue).

Zhang, Y., Rossow, W.B., Lacis, A.A., Oinas, V., Mishchenko, M.I., 2004. Calculation of radiative fluxes from the surface to top of atmosphere based on ISCCP and other global data sets: refinements of the radiative transfer model and the input data. J. Geophys. Res. 109. doi:10.1029/2003JD004457.